

1                   **Statistical characteristics of raindrop size**  
2                   **distribution during rainy seasons in Complicated**  
3                   **Mountain Terrain**

4                   Wenqian Mao<sup>1,3,4</sup>, Wenyu Zhang<sup>2,3,4</sup>, Menggang Kou<sup>2</sup>

5                   1. College of Resources and Environmental Sciences, Gansu Agricultural University, Lanzhou

6                   730070, China

7                   2. School of Geoscience and Technology, Zhengzhou University, Zhengzhou, 450001, China

8                   3. Key Laboratory for Cloud Physics, Chinese Academy of Meteorological Sciences, Beijing

9                   100081, China

10                  4. College of Atmospheric Sciences, Lanzhou University, Lanzhou, 730000, China

11                  Correspondence to: Wenqian Mao (mdycmwq@163.com)

12                  **Abstract:** In order to improve understanding of the characteristics of raindrop size  
13                  distribution (DSD) over complex mountainous terrain, the differences in DSD over the  
14                  southern slopes, northern slopes and interior of the Qilian Mountains were analyzed  
15                  using six months of observations. For all rainfall events, the number concentrations of  
16                  small and large raindrops in the interior and on the southern slopes were greater than  
17                  on the northern slopes, but midsize raindrops were less. The DSD spectrum of the  
18                  interior was more variable and differed significantly from that of the northern slopes.  
19                  The differences in the normalized intercept parameters of the DSD for stratiform and  
20                  convective rainfall were 8.3% and 10.4%, respectively, and those of the mass-weighted  
21                  mean diameters~~mass-weighted diameters~~ were 10.0% and 23.4%, respectively, while  
22                  the standard deviations of DSD parameters at interior sites were larger. The differences  
23                  in the coefficient and exponent of the Z-R relationship were 2.5% and 10.7%,  
24                  respectively, with an increasing value of the coefficient from the southern to the  
25                  northern slopes for stratiform rainfall, but the opposite for convective rainfall. In  
26                  addition, the DSD characteristics and Z-R relationships were more similar at the  
27                  ipsilateral sites and had smaller differences between the southern slopes and interior of  
28                  the mountains.

29                  **Keywords:** raindrop size distribution; complicated mountain terrain; spatial variation  
30  
31

## 32 1 Introduction

33 Raindrop size distribution (DSD), the number of raindrops per drop size per unit  
34 volume, is an important parameter to statistically describe the microstructure of  
35 precipitation (Bringi et al., 2003; Ma et al., 2019a). The measurement of DSD can  
36 provide some fundamental information such as raindrop size ( $D$ ), liquid water content  
37 ( $W$ ), rain rate ( $R$ ), radar reflectivity factor ( $Z$ ) and so on, which has an essential  
38 contribution to improving quantitative precipitation estimation (QPE) using weather  
39 radar and satellite observations (Adirosi et al., 2018; Jash et al., 2019). The  
40 parameterization of DSD can obtain the distribution model parameters of DSD in  
41 different rain types, which is significant in advancing microphysics parameterization in  
42 numerical weather prediction (NWP) models (Wainwright et al., 2014; McFarquhar et  
43 al., 2015; Zhao et al., 2019). In addition, understanding the DSD is crucial in many  
44 applied fields concerning hydrology, agriculture, soil erosion and microwave  
45 communication (Rincon et al., 2002; Smith et al., 2009; Angulo-Martínez et al., 2015;  
46 Lim et al., 2015; Yang et al., 2016).

47 Numerous studies have been carried out on the statistical characteristics of DSD  
48 in different regions (Campos et al., 2006; Seela et al., 2017; Dolan et al., 2018; Protat  
49 et al., 2019; Loh et al., 2019; Jash et al., 2019). It has been shown that the number  
50 concentration and size of raindrops increase with rain rate and so the DSD becomes  
51 higher and wider. The characteristics in different rain types demonstrate that the mass-  
52 weighted mean diameter (i.e.,  $D_m$ ) and normalized intercept parameter (i.e.,  $N_w$ ) of  
53 convective rainfall are larger than those of stratiform rainfall. Furthermore, these  
54 studies also reveal that there are more differences in the characteristics of DSD. Dolan  
55 et al. (2018) divided global DSD characteristics into 6 types by using 12 datasets across  
56 three latitudes and found that the centralized regions and DSD parameters of the 6 types  
57 varied in location. The average number of raindrops in central Korea was usually  
58 greater than that in the southeast under three rainfall systems, especially drops in the  
59 0.31–0.81mm diameter range (Loh et al., 2019). According to DSD measurements in  
60 the Tibetan Plateau region, eastern areas have a higher raindrop number concentration  
61 in the diameter range of 0.437–1.625 mm and greater variation in diameters than in  
62 central areas (Wang et al., 2020). Compared to eastern China and northern China, the  
63 DSD in southern China shows a higher number concentration of relatively small-sized  
64 drops (Zhang et al., 2019). Comparison of the  $Z$ - $R$  relationship (defined as  $Z=AR^b$ )  
65 indicates that the coefficient decreases with increasing  $R$  in the southern Tibetan Plateau,  
66 which is opposite to the case in ~~southern~~*southern* China (Wu et al., 2017). For the DSD  
67 parameters of stratiform and convective rainfall, there are various changes between the  
68 lower and middle reaches of the Yangtze River (Fu et al., 2020).

69 As reported in the above studies, DSD characteristics vary significantly with  
70 factors such as geographical location, climatic region and rain types. Pu et al. (2020)  
71 analyzed the DSD characteristics of five sites in Nanjing city and found the  $N_w$  of DSD  
72 to be largest at site near industrial areas, but the  $D_m$  of DSD was largest at sites near the  
73 city's center. In other words, even at the ~~urban~~*urban*-~~smaller~~*smaller* scale, there are still differences  
74 in the microphysical characteristics reflected by the DSD, which is due to the influence  
75 of the surrounding environment. How, then, do the characteristics of DSD vary from

带格式的: 字体: 倾斜

带格式的: 字体: 倾斜

76 location to location over the complicated mountain terrain? Rao et al. (2006), by  
77 comparing the DSD parameters at different altitudes, suggested that the obvious  
78 variation in DSD with altitude is related to the processes of evaporation and breakup.  
79 Using aircraft observations, Geoffroy et al. (2014) concluded that the total  
80 concentration of raindrops decreased while the average drop size increased with  
81 decreasing altitude. Han et al. (2023) found the rain rate between  $1 \leq R < 5 \text{ mm h}^{-1}$  to  
82 the total precipitation increases with altitude by using the disdrometers data from 2434  
83 m to 4202 m located in the northeastern Tibetan Plateau. With more attention on  
84 mountain research, the concerning question are growing. Such as But how large might  
85 the differences in DSD be at different altitudes in mountainous regions? ~~And~~ and how  
86 significant might the effects be of these differences?

带格式的: 上标

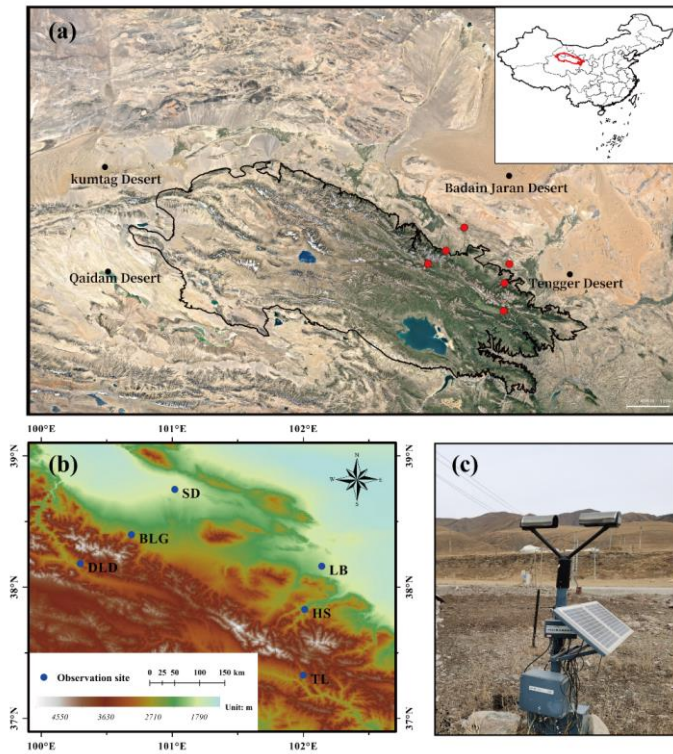
87 The Qilian Mountains, a series of marginal mountains in the northeastern part of  
88 the Tibetan Plateau, are a vitally important ecological protection barrier in the northwest  
89 arid areas of the region, that block the connection between deserts and wilderness  
90 (Figure 1a). The mountains form several inland rivers that are important water sources  
91 for the arid areas of the northwest and have therefore made a considerable contribution  
92 to regional economic development (Gou et al., 2005; Tian et al., 2014; Qin et al., 2016).  
93 In this study, we chose the Qilian Mountains as the research object and selected six sites  
94 with different backgrounds representing the southern slopes, northern slopes and  
95 interior of the mountains. To thoroughly investigate the discrepancies in this complex  
96 mountain terrain, the DSD characteristics and Z-R relationships were comprehensively  
97 analyzed according to different rain types based on continuous disdrometer  
98 observations in the rainy season. The primary goal was to obtain a deeper understanding  
99 and characteristic differences of DSD over the Qilian Mountains and ~~refine~~ improve the  
100 accuracy of QPE comparing with standard Z-R relationships in models, which could  
101 then be used as a research foundation for developing cloud water resources in  
102 mountainous areas.

## 103 2 Data and method

### 104 2.1 Sites and instruments

105 The eastern and middle sections of the Qilian Mountains were chosen as the main  
106 study area, taking into account that several important inland rivers originate from these  
107 areas (Li et al., 2019). Six disdrometers were deployed on the southern slopes, northern  
108 slopes and interior (close to the ridge) of the Qilian Mountains, with three sites in the  
109 eastern section [called Taola (TL, 2910 m), Huangchengshuiguan (HS, 2342 m) and  
110 Liuba (LB, 1926 m), from south to north] and another three sites in the middle section  
111 [called Daladong (DLD, 2957 m), Boligou (BLG, 2455 m) and Shandan (SD, 1765 m),  
112 from south to north]. The background of the Qilian Mountains is shown on the satellite  
113 map in Figure 1a, and the six sites are marked on the topographical map, also in Figure  
114 1b. The distances between the six sites are listed in Table 1. The sites in the south, north  
115 and interior are basically parallel to the orientation of the mountains, and the sections  
116 formed by the sites in the east and interior are basically perpendicular to it. On the basis  
117 of an historical weather review and rain gauge observations, the rainy season at the six  
118 sites is concentrated in May to October, with more precipitation in July, August and

119 September.  
120



121  
122 Figure 1. (a) Geographical overview of the Qian Mountains; (b) the disdrometer sites  
123 (circles); (c) the observation device at TL site. Source: Google Earth © Google Earth  
124 YEAR

125 Table 1. Site details (latitude, longitude, sea level height) and distances (km) between  
126 pairs of sites.

Six sites	LB	HS	TL	SD	BLG	DLD
LB (38.16°N, 102.14°E, 1926m)	-	39.6	94.3	116.0	129.6	161.1
HS (37.83°N, 102.01°E, 2342m)	-	-	55.6	135.1	132.8	154.9
TL (37.33°N, 102.00°E, 2910m)	-	-	-	182.4	167.3	177.0
SD (38.80°N, 101.08°E, 1765m)	-	-	-	-	54.2	96.8
BLG (38.4°N, 100.69°E, 2455m)	-	-	-	-	-	43.3
DLD (38.18°N, 100.3°E, 2957m)	-	-	-	-	-	-

127 This study used an optical, laser-based device to measure the DSD, called a DSG4  
128 disdrometer (Figure 1c), which meets the Functional Specification Requirements for  
129 Disdrometer issued by the China Meteorological Administration. This disdrometer has  
130 an HSC-OTT Parsivel2 sensor as the observation part, manufactured by OTT

131 Messtechnik (Germany) and Huatron (China). When raindrops pass through the  
 132 horizontal flat laser beam generated by the transmitting part of the instrument, it causes  
 133 signal attenuation in the laser observation area. The raindrop size is determined by the  
 134 degree of signal attenuation and the falling speed is recorded by the transit time. The  
 135 sampling time is 60s and the velocity and drop sizes are divided into 32 non-equally  
 136 spaced bins, varying from 0.05 to 20.8 m s<sup>-1</sup> for velocity and 0.062 to 24.5 mm for drop  
 137 diameter.

## 138 2.2 Quality control of the data

139 It was necessary to quality control the data because of potential instrument error.  
 140 Every minute of DSD data collected by the six DSG4 disdrometers from May to  
 141 October 2020 was carefully processed. Specifically, the following criteria were  
 142 employed in choosing data for analysis (Jaffrain et al., 2011; Guyot et al., 2019; Pu et  
 143 al., 2020): (1) the first two size bins were ignored because of low signal-to-noise ratio;  
 144 (2) samples with 1-min total of raindrop number less than 10, or a rain rate at the  
 145 moment of discontinuous observation less than 0.1 mmh<sup>-1</sup> were regarded as noise  
 146 (corresponds to the second sample in Table 2); (3) raindrops with diameters more than  
 147 8 mm were eliminated; (4) raindrops with a falling terminal velocity  $V(D_i)$  that deviated  
 148 from the empirical terminal velocity  $V_{emp}(D_i)$  by more than 40% were removed (Kruger  
 149 and Krajewski, 2002); and (5) samples with less than five bins after the correction of  
 150 falling terminal velocity were deleted because their DSDs could not be determined with  
 151 too few bins. The fourth criterion can be expressed by the formula:

$$152 \quad |V(D_i) - V_{emp}(D_i)| < 0.4V_{emp}(D_i) \quad (1)$$

153 where  $V_{emp}(D_i) = 9.65 - 10.3\exp(-0.6D_i)$  ( $D_i$  is the mean volume-equivalent  
 154 diameter of the  $i$ th size category), as derived from the formula given in Atlas et al.  
 155 (1973).

156 After data quality control, the sample statistics of key steps are shown in Table 2.  
 157 The number of 1-min DSD spectra selected from the six sites (LB, HS, TL, SD, BLG,  
 158 DLD) after data quality control covering the rainy season (May–October) in the Qilian  
 159 Mountains region in 2020 were 11103, 17619, 14814, 10736, 18861 and 13230,  
 160 respectively, which accounted for 87.9%, 85.8%, 84.5%, 91.2%, 80.6% and 86.5% of  
 161 the total number of samples.

162 Table 2. Sample statistics of data quality control at six sites

Samples	LB	HS	TL	SD	BLG	DLD
Total minutes (min)	12625	20536	17526	11770	23401	15289
Total minutes without noise (min)	12602	20509	17494	11756	23371	15267
After quality control (min)	11103	17619	14814	10736	18861	13230
Available <del>data-rain</del> minutes (%)	87.9%	85.8%	84.5%	91.2%	80.6%	86.5%

163

## 164 2.3 Integral parameters of rainfall

165 The basic observations obtained by the disdrometer were the counts of raindrops  
 166 at each diameter and velocity. Also, the diameters given by the disdrometers were the

167 mid value of two adjacent bins, which we take as the corresponding endpoint bin values.  
 168 The velocities were the weighted average velocity class over the corresponding  
 169 disdrometer. The raindrop number concentration  $N(D_i)$  ( $\text{m}^{-3} \text{mm}^{-1}$ ) in the  $i$ th size bin  
 170 per unit volume per unit size interval for diameter was calculated by the following  
 171 equation:

$$172 \quad N(D_i) = \sum_{i,j=1}^{32} \frac{n_{i,j}}{A \cdot \Delta t \cdot V_j \cdot \Delta D_i} \quad (2)$$

173 where  $n_{i,j}$  denotes the counts of raindrops measured by the disdrometer within size bin  
 174  $i$  and velocity bin  $j$  during the sampling time  $\Delta t$ ;  $A$  and  $\Delta t$  are the sampling area ( $0.0054$   
 175  $\text{m}^2$ ) and sampling time ( $60$  s), respectively;  $V_j$  ( $\text{m s}^{-1}$ ) is the mid-value falling speed for  
 176 velocity bin  $j$ ; and  $\Delta D_i$  is the diameter spread for the  $i$ th diameter bin.

177 Some integral rainfall parameters, such as the total number concentration  $N_t$  ( $\text{m}^{-3}$ ),  
 178 rain rate  $R$  ( $\text{mm h}^{-1}$ ), radar reflectivity factor  $Z$  ( $\text{mm}^6 \text{m}^{-3}$ ) and liquid water content  $W$   
 179 ( $\text{g cm}^{-3}$ ), can be derived by the following equations:

$$180 \quad N_t = \sum_{i=1}^{32} N(D_i) \Delta D \quad (3)$$

$$181 \quad R = \frac{6\pi}{10^4 \rho_w} \sum_{i=1}^{32} V(D_i) D_i^3 N(D_i) \Delta D_i \quad (4)$$

$$182 \quad Z = \sum_{i=1}^{32} N(D_i) D_i^6 \Delta D_i \quad (5)$$

$$183 \quad W = \frac{\pi \rho_w}{6 \times 10^3} \sum_{i=1}^{32} D_i^3 N(D_i) \Delta D_i \quad (6)$$

184 where  $\rho_w$  is the water density ( $1.0 \text{ gcm}^{-3}$ ); and  $V(D_i)$  is the falling speed from the  
 185 disdrometer. In this study, when calculating the rain rate we use  $V_{emp}(D_i)$  to replace  $V(D_i)$   
 186 because of measurement error, particularly at larger bins and faster falling speeds,  
 187 [which is inspired from Tokay et al. \(2014\) and Zhang et al. \(2019\)](#).

188 The characteristics of DSD can be described by a three-parameter gamma  
 189 distribution in the form introduced by Ulbrich (1983). Also, it has better fitting  
 190 capability than the M-P distribution on the broader variation of DSD fluctuations,  
 191 including the middle rain drops, especially on small and large rain scales. The three-  
 192 parameter gamma distribution can be expressed by the following formula:

$$193 \quad N(D) = N_0 D^\mu \exp(-\Lambda D) \quad (7)$$

194 where  $N(D)$  is the raindrop number concentration;  $D$  is the raindrop bins with unit  $\text{mm}$ ;  
 195 and  $N_0$ ,  $\mu$  and  $\Lambda$  are the intercept, shape and slope parameter from the three parameters  
 196 of the gamma model, which can be derived from gamma moments or the least-squares  
 197 method, respectively. When  $\mu=0$ , it degenerates into the M-P DSD model.

198 Although, the gamma distribution is commonly accepted, the normalized gamma  
 199 distribution has also been widely adopted with its independent parameters and clear  
 200 physical meaning as follows (Dolan et al., 2018; Ma et al., 2019):

$$N(D) = \frac{3}{128} N_w \left[ \frac{(4 + \mu)^{(4+\mu)}}{\Gamma(4 + \mu)} \right] \left( \frac{D}{D_m} \right)^\mu \exp \left( -\frac{(4 + \mu)D}{D_m} \right) \quad (8)$$

where  $\mu$  is the shape parameter, which is in dimensionless;  $D_m$  (mm) is the mass-weighted mean diameter, and  $N_w$  ( $\text{m}^{-3} \text{mm}^{-1}$ ) is the normalized intercept parameter computed from  $D_m$ . The form is as follows:

$$D_m = \frac{\sum_{i=1}^{32} N(D_i) D_i^4 \Delta D_i}{\sum_{i=1}^{32} N(D_i) D_i^3 \Delta D_i} \quad (9)$$

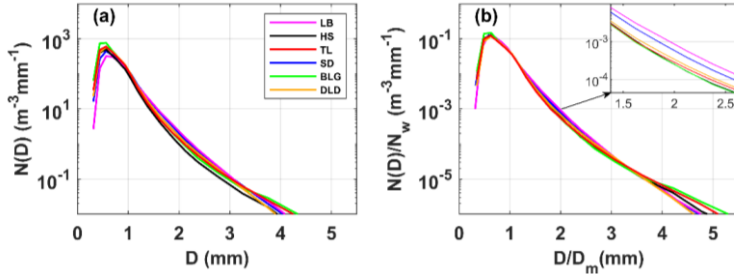
$$N_w = \frac{4^4}{\pi \rho_w} \left( \frac{10^3 W}{D_m^4} \right) \quad (10)$$

### 3 DSD parameter characteristics

#### 3.1 Characteristics of DSD

Figure 2a shows the mean DSDs for the six sites during the rainy season in the Qilian Mountains. The maximum concentration of raindrops was around 0.562 mm in diameter and the maximum number concentration values of sites were order as follows: BLG>TL>DLD>HS>SD>LB. As the diameter increased, the number concentration decreased and the concentration values followed the order LB>SD>DLD>TL>BLG>HS at around 2 mm in diameter. When the diameter was larger than 4 mm, the concentration at TL, BLG and HS was relatively high. In this study, the data were roughly divided into small raindrops (less than 1 mm in diameter), midsize raindrops (1–3 mm) and large raindrops (greater than 3 mm) to easily describe the difference in DSDs (Ma et al., 2019b; Pu et al., 2020). To highlight the DSD differences caused by the background environment, Figure 2b shows the mean DSDs normalized by the  $N_w$  and  $D_m$  results for the sites. Compared with Figure 2a, the raindrop characteristics were more consistent across sizes, while the differences between the sites were more pronounced, especially in the midsize and large raindrops, which truly reflected the DSD differences caused by the location. Combining the characteristics of the geographical environment of the six sites, we can analyze some differences in DSD characteristics in the Qilian Mountains. For small raindrops, the number concentrations at interior and southern-slope sites were greater than at northern-slope sites; for midsize raindrops, the number concentrations decreased sequentially at the northern-slope, southern-slope and interior sites; and for large raindrops, the number concentrations at the interior sites were larger. In addition, the number concentrations of raindrops in the middle section of this the mountainous area were slightly greater than those in the eastern section.

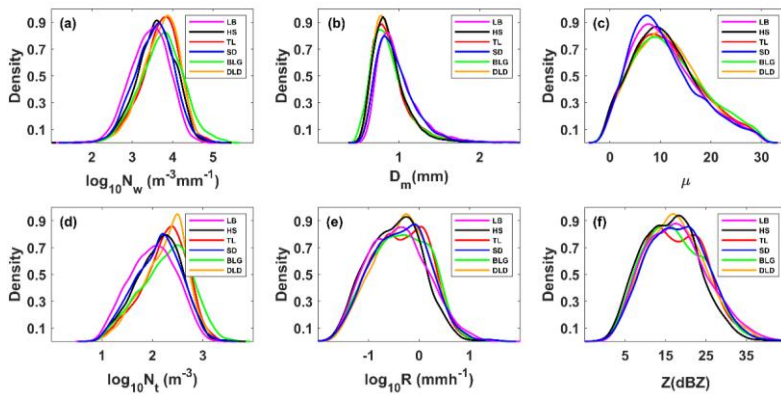




232  
 233 Figure 2. The (a) mean and (b) normalized mean DSDs at six sites in the Qilian  
 234 Mountains region in the rainy season

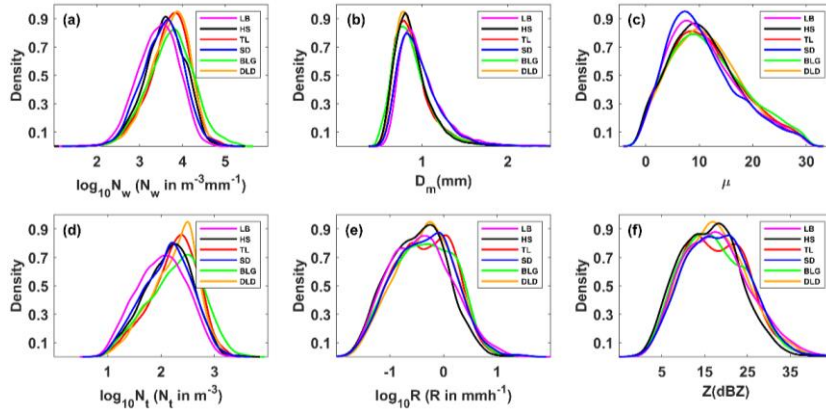
235 **3.2 Distribution of DSD parameters**

236 In order to study the differences in DSDs, we selected six integral rainfall  
 237 parameters for discussion—namely, the normalized intercept parameter ( $N_w$ ), mass-  
 238 weighted mean diameter ( $D_m$ ), shape parameter ( $\mu$ ), total number concentration ( $N_t$ ),  
 239 rain rate ( $R$ ) and radar reflectivity factor ( $Z$ ). Figure 3 and Table 3 show the distributions  
 240 and statistics of these six DSD parameters (the distribution of each was normalized  
 241 using the uniform method). On average,  $D_m$  was more concentrated on smaller values  
 242 at HS and BLG, which showed smaller mean values than TL and DLD but significantly  
 243 more values greater than 1 mm at LB and SD;  $\log_{10}N_w$  was more centralized on larger  
 244 values at TL and DLD, with relatively smaller values at LB and SD; and the distribution  
 245 patterns for  $\mu$  and  $\log_{10}N_t$  were similar to those for  $\log_{10}N_w$ . The density curves of  $R$  and  
 246  $Z$  were similar, but there were differences among the six sites, which are analyzed in  
 247 detail later in the paper. It is noteworthy that the frequency of samples with  $R$  around  
 248 0.6–1.0 mm h<sup>-1</sup> was highest, and samples with  $R$  less than 1 mm h<sup>-1</sup> accounted for more  
 249 than half of the total rainfall.



250





251

252 Figure 3. Probability density distribution of integral DSD parameters at six sites (LB,  
 253 HS, TL, SD, BLG, DLD): (a) normalized intercept parameter  $\log_{10}N_w$  ( $N_w$  in  $m^{-3}mm^{-1}$ );  
 254 (b) mass-weighted mean diameter  $D_m$  (mm); (c) shape parameter  $\mu$ ; (d) total number  
 255 concentration  $\log_{10}N_t$  ( $N_t$  in  $m^{-3}$ ); (e) rain rate  $\log_{10}R$  ( $R$  in  $mm h^{-1}$ ); (f) radar reflectivity  
 256 factor  $Z$  (dBZ)

257 Table 3. Statistical of several integral DSD parameters for all observations at six sites  
 258 (LB, HS, TL, SD, BLG, DLD).

Sites	$\log_{10}N_w$ ( $m^{-3}mm^{-1}$ )			$D_m$ (mm)			$\mu$			$\log_{10}N_t$ ( $m^{-3}$ )			$R$ ( $mm h^{-1}$ )			$Z$ (带格式的: 居中)		
	ME	SD	SK	ME	SD	SK	ME	SD	SK	ME	SD	SK	ME	SD	SK	ME	SD	SK
LB	3.43	0.47	-0.25	0.99	0.29	2.68	10.92	6.63	0.61	2.01	0.46	-0.07	0.94	1.90	0.23	17.79	7.82	0.44
HS	3.59	0.48	-0.29	0.89	0.25	3.35	11.12	6.64	0.53	2.13	0.45	-0.22	0.69	1.60	0.05	16.24	7.08	0.34
TL	3.69	0.48	-0.55	0.90	0.29	4.49	11.37	6.84	0.48	2.23	0.44	-0.43	0.89	1.48	-0.05	17.47	7.55	0.35
SD	3.54	0.48	-0.17	0.96	0.26	2.12	10.62	6.61	0.71	2.11	0.46	-0.17	0.97	2.01	0.06	17.95	7.47	0.28
BLG	3.72	0.54	-0.15	0.89	0.29	5.17	11.71	7.06	0.46	2.26	0.50	-0.25	0.94	2.13	-0.04	17.34	7.66	0.41
DLD	3.69	0.45	-0.50	0.90	0.25	2.66	11.52	6.66	0.43	2.24	0.43	-0.46	0.95	1.62	-0.01	17.70	7.43	0.37

259 Note: ME is mean; SD is standard deviation; SK is skewness.

### 260 3.3 DSD characteristics in different rain rate classes

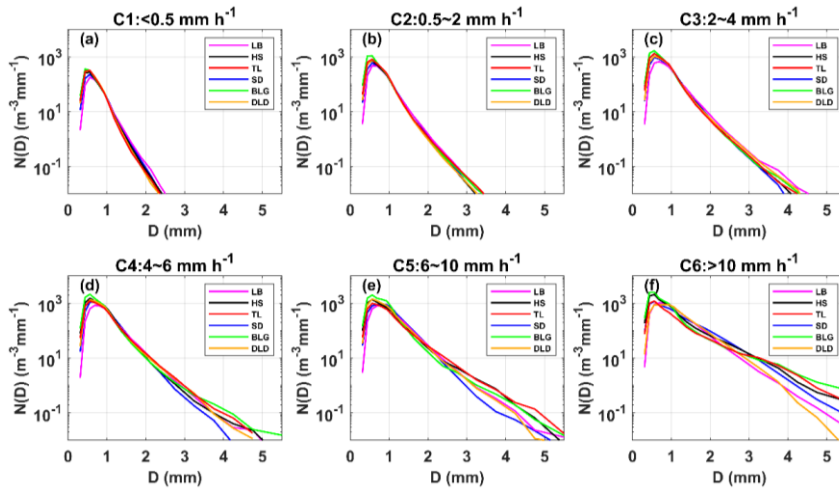
261 To further understand the characteristics of DSDs at the six sites, the samples were  
 262 divided into six classes according to the associated rain rates ( $R$ ): C1,  $R < 0.5$ ; C2,  
 263  $0.5 \leq R < 2$ ; C3,  $2 \leq R < 4$ ; C4,  $4 \leq R < 6$ ; C5,  $6 \leq R < 10$ ; C6,  $R \geq 10$   $mm h^{-1}$ . This classification  
 264 was based on two considerations: firstly, the number of observation samples in different  
 265 rainfall rates roughly conformed to a normal distribution; and secondly, the mean  
 266 maximum diameter interval of different rainfall rates gradually increased (Li et al.,  
 267 2019). Of course, other classification studies were referenced and the fact that the rain  
 268 rate in this area is smaller than that in southern China was taken into account (Ma et al.,  
 269 2019b; Zeng et al., 2021). Figure 4 shows the mean DSDs at each rainfall rate class for  
 270 the six sites. Table 4 lists the number of samples and statistical values of the DSD

271 parameters for the six classes. Clearly, as the rainfall rate increased, the number  
 272 concentration of almost all raindrop sizes and the width of DSD shapes increased, and  
 273 thus the tail of the DSD shape moved gradually towards a larger diameter, similar to  
 274 previous findings, such as those of Ma et al. (2019b) and Pu et al. (2020). Taking a  
 275 number concentration of  $0.01 \text{ m}^{-3}\text{mm}^{-1}$ , the mean maximum diameter of DSD in each  
 276 class was ordered as follows: 2.3–2.5, 3.2–3.4, 3.9–4.5, 4.3–5.0, 5.0–5.6 and 6.0–7.0  
 277 mm (the sixth-class diameter range is not fully shown in the figure). In class C1, the  
 278 number concentrations were relatively similar at different sites; starting from class C2,  
 279 the differences in number concentration increased when the diameter was greater than  
 280 2 mm for the six sites; and the differences of in number concentration were gradually  
 281 reflected in each raindrop size bin as the rainfall rate class increased. Observationally,  
 282 the DSDs of BLG, HS and TL had larger number concentrations in different rainfall  
 283 rate classes, and the DSD parameters and standard deviations (SDs) were larger,  
 284 especially for BLG.

285 Table 4. Statistics of several integral DSD parameters for six rain rate classes at six sites.

Class	Sites	Samples	$\log_{10}N_w$		$D_m$		$\mu$		$\log_{10}N_r$		$R$		$Z$	
			$(\text{m}^{-3}\text{mm}^{-1})$		$(\text{mm})$				$(\text{m}^{-2})$		$(\text{mm h}^{-1})$		$\text{dBZ}$	
			ME	SD	ME	SD	ME	SD	ME	SD	ME	SD	ME	SD
C1(<0.5 mm h <sup>-1</sup> )	LB	6520	3.25	0.41	0.88	0.18	12.36	7.09	1.74	0.34	0.20	0.13	12.68	4.52
	HS	10753	3.43	0.44	0.81	0.17	12.01	7.03	1.89	0.37	0.20	0.13	11.90	4.54
	TL	7858	3.52	0.44	0.79	0.16	12.91	7.12	1.96	0.37	0.20	0.13	11.78	4.16
	SD	5772	3.34	0.43	0.85	0.18	11.72	6.99	1.82	0.36	0.20	0.13	12.51	4.40
	BLG	10073	3.50	0.48	0.79	0.17	12.94	7.28	1.94	0.40	0.20	0.13	11.73	4.26
	DLD	6891	3.51	0.43	0.79	0.15	13.04	6.92	1.96	0.36	0.21	0.13	12.14	4.15
C2(0.5–2 mm h <sup>-1</sup> )	LB	3318	3.66	0.41	1.06	0.24	9.93	5.75	2.30	0.28	1.00	0.41	22.55	3.27
	HS	5700	3.82	0.39	0.97	0.21	10.21	5.88	2.44	0.26	0.96	0.37	21.67	3.09
	TL	5368	3.87	0.42	0.98	0.23	10.35	6.15	2.49	0.26	1.07	0.41	22.18	3.33
	SD	3778	3.73	0.41	1.03	0.23	9.94	6.14	2.36	0.28	1.02	0.40	22.40	3.15
	BLG	6411	3.97	0.47	0.94	0.25	11.24	6.72	2.56	0.30	1.07	0.43	21.69	3.69
	DLD	4778	3.88	0.37	0.95	0.20	10.91	6.02	2.47	0.24	1.01	0.40	21.60	3.19
C3(2–4 mm h <sup>-1</sup> )	LB	782	3.71	0.47	1.31	0.37	7.33	4.28	2.52	0.29	2.77	0.56	29.54	2.87
	HS	884	3.96	0.50	1.16	0.34	8.42	5.22	2.73	0.27	2.76	0.54	28.33	3.06
	TL	1232	4.00	0.47	1.13	0.33	8.70	5.93	2.75	0.23	2.68	0.53	28.07	3.16
	SD	812	3.89	0.44	1.19	0.27	8.57	5.53	2.63	0.26	2.71	0.53	28.41	2.68
	BLG	1865	4.05	0.49	1.11	0.30	8.62	5.75	2.81	0.25	2.70	0.53	27.99	3.29
	DLD	1111	3.91	0.44	1.18	0.29	7.81	5.45	2.70	0.23	2.74	0.54	28.73	3.09
C4(4–6 mm h <sup>-1</sup> )	LB	229	3.80	0.47	1.41	0.40	7.33	3.94	2.65	0.31	4.76	0.57	32.69	2.63
	HS	191	4.03	0.54	1.28	0.47	7.54	4.42	2.86	0.27	4.80	0.56	31.70	3.34
	TL	213	3.84	0.56	1.41	0.51	6.23	4.64	2.77	0.28	4.77	0.54	32.82	3.54
	SD	187	4.03	0.41	1.24	0.27	8.35	5.02	2.80	0.22	4.76	0.54	31.32	2.52
	BLG	321	3.99	0.66	1.33	0.53	7.97	6.10	2.93	0.27	4.78	0.54	32.44	4.40
	DLD	270	3.92	0.53	1.35	0.47	6.50	4.80	2.83	0.25	4.83	0.56	32.55	3.47
C5(6–10 mm h <sup>-1</sup> )	LB	167	3.81	0.46	1.55	0.44	6.46	3.38	2.72	0.27	7.66	1.22	35.74	2.85

C6(>10 mm h <sup>-1</sup> )	HS	49	3.69	0.74	1.70	0.68	6.89	4.82	2.75	0.38	7.42	1.09	36.14	4.29
	TL	103	3.57	0.62	1.78	0.66	5.20	4.62	2.71	0.32	7.32	1.02	37.03	3.76
	SD	128	3.96	0.39	1.42	0.35	7.10	3.96	2.82	0.21	7.68	1.17	34.76	2.42
	BLG	138	3.97	0.76	1.51	0.80	8.34	6.35	2.99	0.27	7.37	1.02	35.09	4.96
	DLD	122	3.90	0.46	1.46	0.34	6.13	4.20	2.86	0.26	7.29	1.11	35.32	2.88
	LB	87	3.85	0.44	1.73	0.53	5.08	3.05	2.87	0.32	14.81	7.57	39.58	3.57
	HS	42	3.60	0.65	2.19	0.92	6.74	5.27	3.00	0.28	21.69	9.91	42.93	6.11
	TL	40	3.16	0.69	2.69	1.19	4.34	5.20	2.74	0.32	18.25	9.69	44.70	5.41
	SD	59	3.66	0.29	2.04	0.46	3.30	2.48	2.91	0.16	21.07	8.34	42.85	4.10
	BLG	53	3.38	0.93	2.58	1.52	5.58	6.19	3.00	0.37	21.95	9.05	44.08	7.50
	DLD	58	3.82	0.47	1.80	0.46	6.64	4.12	2.84	0.28	16.58	7.21	40.13	3.53



286

287 Figure 4. Distribution of mean measured DSD for different rain rate classes at six sites.

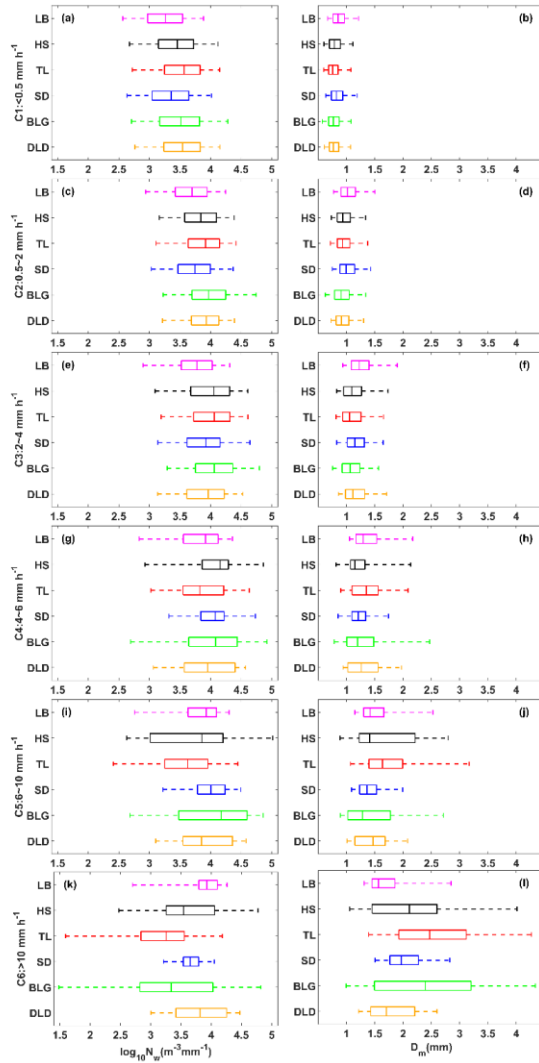
288 Figure 5 shows box-and-whisker plots of the normalized intercept parameter  
 289  $\log_{10}N_w$  and mass-weighted mean diameter  $D_m$  for six sites in each rain rate class. The  
 290 middle line in the box indicates the median. The left and right lines indicate the 25<sup>th</sup> and  
 291 75<sup>th</sup> percentiles. The left and right ends of whiskers indicate the most extreme data  
 292 points between the 5<sup>th</sup> and 95<sup>th</sup> percentiles, except outliers. The median  $D_m$  gradually  
 293 increased with a larger value range as the rain rate class increased, particularly for HS  
 294 and BLG in class C5 and C6. The median  $\log_{10}N_w$  increased in class C1 to C3 and then  
 295 tended to decrease in class C5 to C6, for which the reduction was obvious at sites with  
 296 a larger value range, such as HS and BLG. Ma et al. (2019b) also obtained similar  
 297 conclusions about  $D_m$  and  $\log_{10}N_w$  that  $D_m$  values increase with the increased rainfall  
 298 intensity, while the  $\log_{10}N_w$  is not as clear. The indication was that the increase in rain  
 299 rate was mainly due to the growth in raindrop size. Also, the change in number  
 300 concentration may have been caused by the imbalance between the loss of number  
 301 concentration at small raindrop size and the addition at large raindrop sizes, which in a  
 302 sense implies a relationship between the collision-coalescence and break-up of  
 303 raindrops. It is worth noting that the microphysical processes were quite different

带格式的: 下标

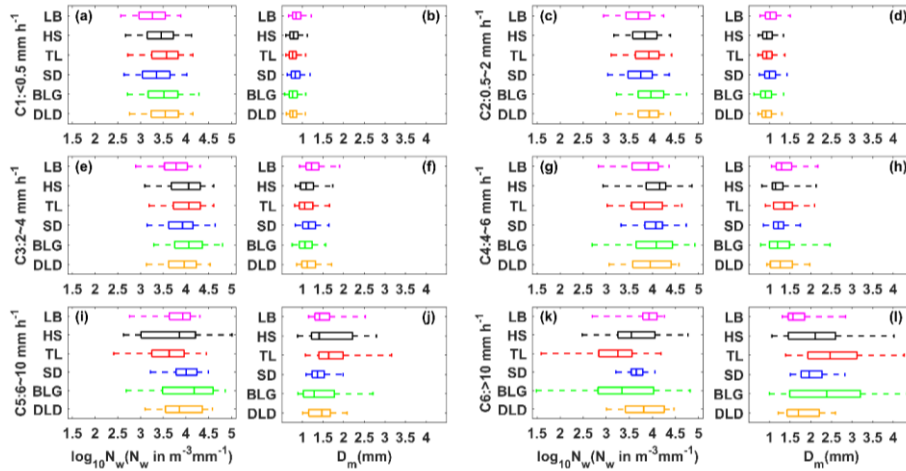
带格式的: 下标

带格式的: 下标

304 among the sites, being greatly influenced by the surrounding environment. Because HS  
 305 and BLG were located in the interior of the mountains and close to the ridge, their  
 306 dynamics and thermodynamics as well underlying surfaces were thus different from  
 307 those of other sites.



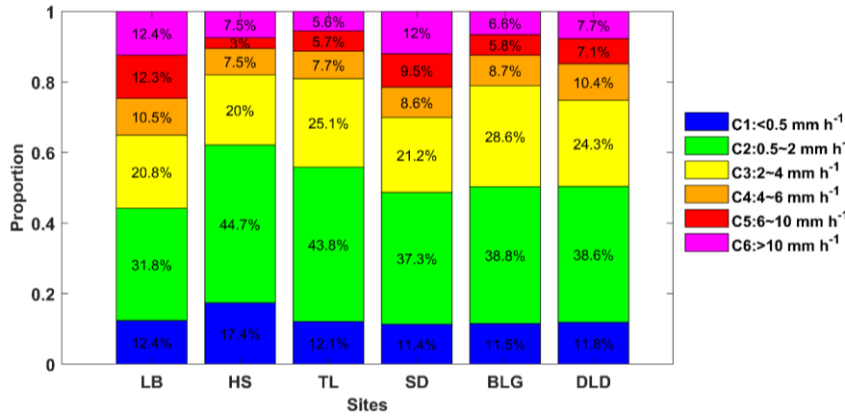
308



309

310 Figure 5. Variation of the normalized intercept parameter  $\log_{10}N_w$  (a) and the mass-  
 311 weighted mean diameter  $D_m$  (b) for different rain rate classes at six sites. The three lines  
 312 in the boxes are the 25<sup>th</sup>, 50<sup>th</sup> and 75<sup>th</sup> percentiles, from left to right, respectively. The  
 313 whiskers at the left and right ends are the 5<sup>th</sup> and 95<sup>th</sup> percentiles, respectively. The  
 314 colors represent the six sites as in other figures.

315 Figure 6 displays the contribution of different rain rate classes to the total rainfall  
 316 at different sites. It is clear that C2 contributed the most to the total rainfall of all sites,  
 317 followed by C3, and the sum of the two classes' contribution could reach 60% of the  
 318 total rainfall. Compared with the interior and southern-slope sites, C2 and C3  
 319 contributed slightly less to sites LB and SD (i.e., the northern slopes), while C5 and C6  
 320 contributed relatively more to sites LB and SD, indicating that there is a greater  
 321 probability of heavy precipitation events on the northern slopes. The DSD parameters  
 322 in Table 3 provide a more detailed representation of the rainfall differences between the  
 323 three geographical sections of the Qilian Mountains, i.e., the interior, southern slopes  
 324 and northern slopes. Meanwhile, it also reflects the characteristics of rainfall in the  
 325 eastern and interior sections, such as the eastern section had larger  $Z$  and  $D_m$  and smaller  
 326  $\log_{10}N_w$  and  $\log_{10}N_t$  compared to the interior. It is possible that there is a certain spatial  
 327 connection between precipitation at the sites, related to factors such as the source of  
 328 precipitation vapor, weather system and so on.



329

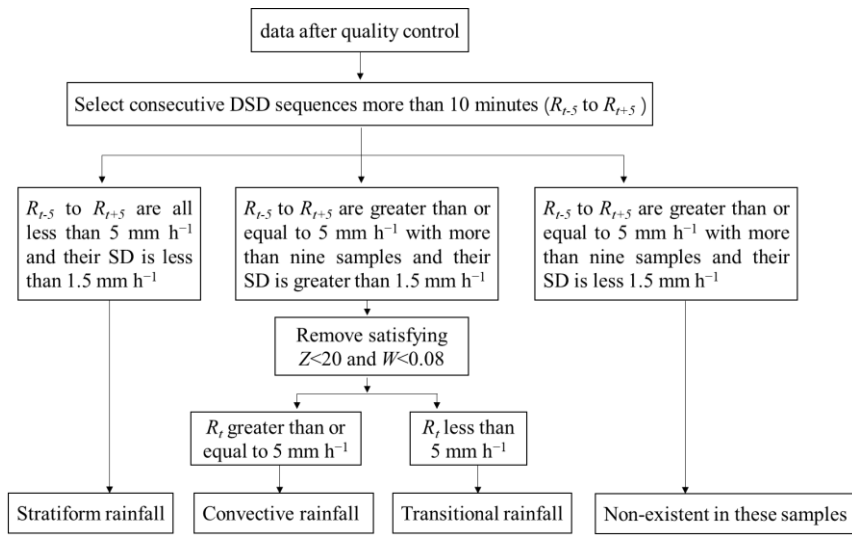
330 Figure 6. Proportion of rainfall with different rain rate classes to rain amount at six sites.

### 331 3.4 DSD properties for different rain types

332 Previous studies on DSD have shown that there are significant differences in the  
 333 DSD of convective and stratiform rainfall in the same climatic region, which has a  
 334 substantial impact on the parameterization of NWP and remote sensing observations  
 335 (Bringi et al., 2003; Penide et al., 2013). Due to the different physical mechanisms of  
 336 convective and stratiform rainfall, it is possible to discuss the differences in  
 337 microphysical structures for rainfall types through their DSD. Studies have employed  
 338 many different classification methods for rainfall types; example, Testud et al. (2001)  
 339 used the rain rate; Chen et al. (2013) combined the rain rate and its SD; and the findings  
 340 of Das et al. (2018) were based on the rain rate and radar reflectivity factor. Among  
 341 these, the method of Chen et al. (2013) has commonly been used to establish samples  
 342 of convective and stratiform rainfall, but mainly in semi-humid or humid regions with  
 343 relatively high rain rate and rainfall. However, the Qilian Mountains are located in the  
 344 semi-arid regions of China and far from the sea, where the average rainfall rain and  
 345 rainfall are quite different from in semi-humid regions. Therefore, this paper proposes  
 346 a new classification method for precipitation applicable to the arid and semi-arid  
 347 regions of Northwest China based on the classification ideas of Chen et al. (2013) and  
 348 Das et al. (2018).

349 Firstly, the sequences of DSD with continuous 1-min samples more than 10 min  
 350 are determined, and  $R_t$  is defined as the rain rate at time  $t$ . In the first case, the  $R$  of  
 351 samples from  $R_{t-5}$  to  $R_{t+5}$  are all less than  $5 \text{ mm h}^{-1}$  and their SD is less than  $1.5 \text{ mm h}^{-1}$ ;  
 352 in the second case, the  $R$  of samples from  $R_{t-5}$  to  $R_{t+5}$  are greater than or equal to  $5$   
 353  $\text{mm h}^{-1}$  with more than nine samples and their SD is greater than  $1.5 \text{ mm h}^{-1}$ ; and in  
 354 the third case, the situation is the same as the second case but their SD is less  $1.5$   
 355  $\text{mm h}^{-1}$ . Secondly, samples satisfying  $Z < 20$  and  $W < 0.08$  in the second case are removed  
 356 (Thurai et al., 2016; Das et al., 2018). And then, samples with  $R_t$  greater than or equal  
 357 to  $5 \text{ mm h}^{-1}$  in the second case are regarded as convective rainfall and samples with  $R_t$   
 358 less than  $5 \text{ mm h}^{-1}$  in the second case are regarded as transitional rainfall (the rainfall

359 stage in which convective precipitation develops and declines). Samples in the first case  
 360 are regarded as stratiform rainfall. Through experiments, the third case does not exist.  
 361 The main calculation process is shown in Figure 7



362  
 363 Figure 7. Classification method for rainfall types in the Qilian Mountains.

364 The  $\log_{10}N_w$  and  $D_m$  of different rainfall types were different, which were taken as  
 365 the main research objects. Figure 7-8 shows the variation of  $\log_{10}N_w$  with  $D_m$  at different  
 366 sites. The blue, red and yellow scatter points represent stratiform, convective and  
 367 transitional rainfall, respectively. Obviously, there are fairly clear boundaries between  
 368 the scatter points for the different precipitation type events, and the same dividing line  
 369 can be used to distinguish between the different rainfall types at different sites. The  
 370 ~~green~~ solid lines were drawn based on visual examination of the data with a slope  
 371 of approximately  $-1.60$  and intercept of  $6.008$  to represent the split between stratiform,  
 372 transitional and convective rainfall in all subplots. The ~~black-green~~ dashed line can  
 373 distinguish transitional rainfall (transitional and stratiform rainfall have an overlap area)  
 374 with a slope of approximately  $-3.338$  and intercept of  $6.847$ . Note that the dividing line  
 375 between stratiform and convective rainfall has the same slope as that obtained by Bringi  
 376 et al. (2003) (solid green line with a slope of  $-1.6$  and intercept of  $6.3$ ), who fitted  
 377 composite results based on disdrometer data and from radar retrievals covering many  
 378 climate conditions from near the equator to plateau. The  $\log_{10}N_w$  and  $D_m$  from the  
 379 figures for stratiform, convective and transitional rainfall are respectively concentrated  
 380 in the ranges of  $3.1-3.9\text{-m}^{-3}\text{mm}^{-1}$ ,  $0.75-1.1\text{ mm}$ ;  $3.8-4.2\text{-m}^{-3}\text{mm}^{-1}$ ,  $1.4-1.6\text{ mm}$ ;  $3.6-$   
 381  $4.0\text{-m}^{-3}\text{mm}^{-1}$ ,  $1.05-1.2\text{ mm}$ . Compared to the maritime-like cluster and continental-like  
 382 cluster of convective rainfall proposed by Bringi et al. (2003), the convective events in  
 383 the Qilian Mountains are ~~not belong to more consistent with the~~ continental-like cluster  
 384 ~~or maritime-like cluster~~ (the gray rectangle with smaller  $\log_{10}N_w$  and larger  $D_m$  in Fig.  
 385 7), while the averages of  $D_m$  are slightly less than the continental-like cluster and the

带格式的: 居中, 缩进: 首行缩进: 0 字符, 段落间距  
段前: 0.5 行, 段后: 0.5 行

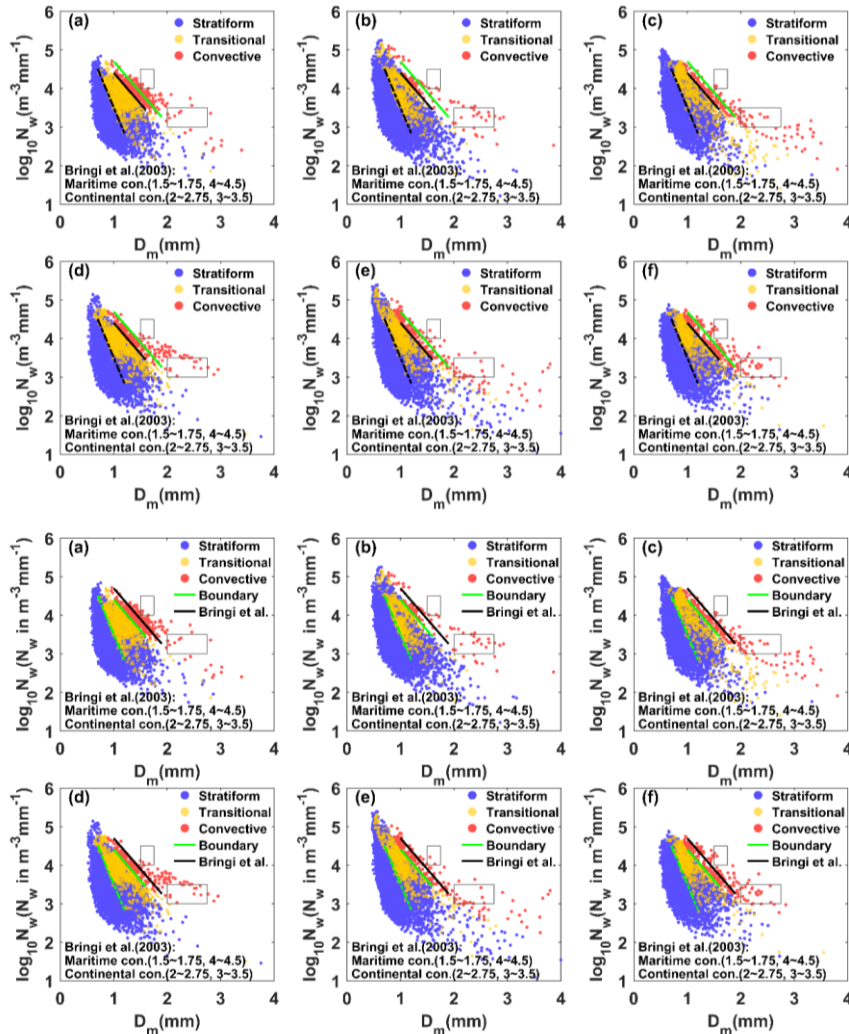
带格式的: 字体: 倾斜

带格式的: 字体: 倾斜, 下标



386 averages of  $\log_{10}N_w$  are greater than the continental-like cluster. There are isolated  
 387 convective events in the maritime-like cluster, but it is difficult to have more events  
 388 from the trend between  $\log_{10}N_w$  and  $D_m$ . This is also consistent with the features of the  
 389 geographical location of the Qilian Mountains.

带格式的: 字体: 非倾斜

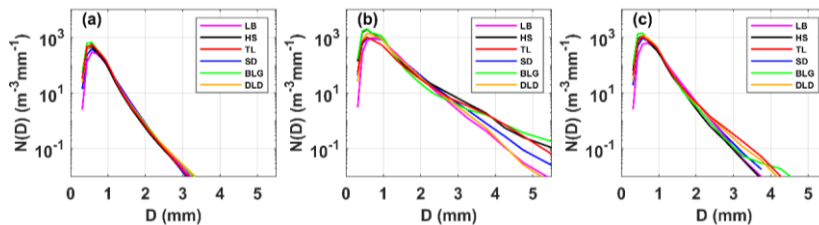


390

391  
 392 Figure 87. Scatter plot of  $\log_{10}N_w$  versus  $D_m$  for different rain types at (a) LB, (b) HS,  
 393 (c) TL, (d)SD, (e)BLG, and (f)DLD. The stratiform cases, convective cases and  
 394 transitional cases are represented by blue, red and yellow scatter points, respectively.  
 395 The black-green dashed lines are the  $\log_{10}N_w$ - $D_m$  relationship for stratiform versus  
 396 convective cases and stratiform versus transitional case. The black dashed lines are the  
 397  $\log_{10}N_w$ - $D_m$  relationship for stratiform versus convective cases and stratiform versus  
 398 transitional case from Bringi et al. (2003). The green dotted lines are the area of overlap

399 [between stratiform and transitional case.](#)

400 Figure 8-9 shows the mean DSDs for stratiform, convective and transitional  
401 rainfall at the six sites. The range of number concentrations and corresponding raindrop  
402 diameters for the three types were significantly different, matching the basic  
403 characteristics of DSD. The mean DSDs of stratiform rainfall differed slightly among  
404 the sites; convective rainfall had big differences at among the sites; and transitional  
405 rainfall presented more differences beginning at larger than 2.2 mm in diameter, which  
406 were the expected results. Stratiform rainfall usually has a large horizontal extent and  
407 an homogeneous cloud distribution, which makes the DSD characteristics basically the  
408 same under the influence of the same cloud system in mountainous areas. However,  
409 convective rainfall is related to local thermal and dynamical factors, which could lead  
410 to differences in DSD at different sites when considering the complex topography and  
411 diverse underlying surfaces in mountainous areas. For example, for convective rainfall,  
412 there was a significant increase in the number concentration of raindrops larger than 2.2  
413 mm in diameter at BLG, HS and TL, indicating that these sites are conducive to the  
414 development of convective precipitation. Also, the number concentration of small  
415 raindrops at BLG and HS were higher than at TL (the southern slope), which may be  
416 due to the higher altitude of the interior sites reducing the falling distance of raindrops  
417 after exiting the cloud and decreasing the impact of collision on the raindrop evolution.  
418 In other words, even for the same rainfall type, the microphysics of rainfall at different  
419 sites is still different, depending on the topography and position of the observation point  
420 relative to the cloud base.



421  
422 Figure 98. Distribution of mean measured DSD for (a) stratiform rainfall, (b) convective  
423 rainfall and (c) transitional rainfall at six sites.

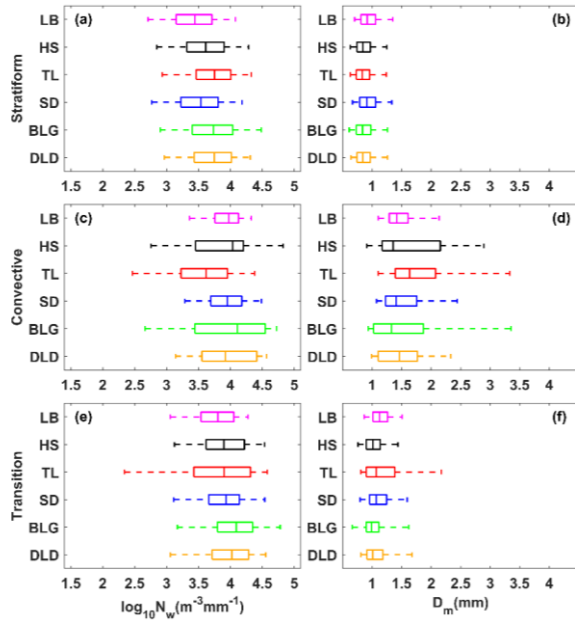
424 Figure 9-10 shows box-and-whisker plots of  $\log_{10}N_w$  and  $D_m$  for different rain types.  
425 The  $\log_{10}N_w$  and  $D_m$  of stratiform rainfall were smaller than those of convective rainfall  
426 but larger than those of transitional rainfall. Sites with a large  $\log_{10}N_w$  value range had  
427 larger value ranges for  $D_m$ ; and sites with a large median  $\log_{10}N_w$  had a smaller median  
428  $D_m$ , especially at sites HS and BLG for convective rainfall. Based on the mean values  
429 of the six sites in Table 5, the DSD characteristics in the Qilian Mountains consist of a  
430 larger  $N_w$  and smaller  $D_m$  ([compared the results of studies in other regions, seeing](#)  
431 [discussion section for details](#)) due to the melting of tiny, compact graupel, and rimed  
432 ice particles (relative to large, low-density snowflakes). Compared with transitional  
433 rainfall, the  $D_m$  of convective rainfall was obviously larger, indicating that the increase  
434 in rain rate in this area is mainly due to the growth in raindrop size. Moreover, on the

435 northern slopes one should consider the increase in number concentration, because the  
 436  $\log_{10}N_w$  of convective rainfall also increased. Note that the number of convective  
 437 samples on the northern slopes was higher than that of other sites, which corresponds  
 438 to the speculation regarding the contribution of different rain rate classes. On average,  
 439 for stratiform rainfall, the dispersion degree of  $\log_{10}N_w$  and  $D_m$  at different sites was  
 440 8.3% and 10.0%, respectively; and for convective rainfall it was 10.4% and 23.4%. The  
 441 SDs of DSD parameters at sites HS and BLG were relatively large.

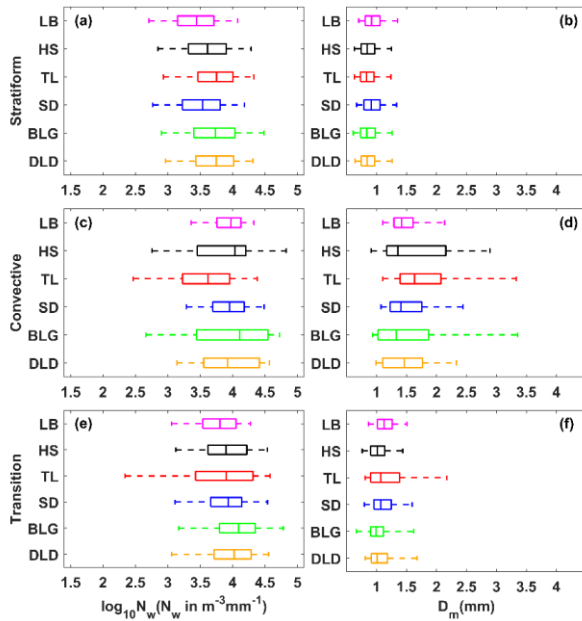
442 Table 5 Statistics of several integral DSD parameters for six sites with stratiform rainfall,  
 443 convective rainfall and transitional rainfall

Type	Sites	No. samples	$\log_{10}N_w$		$D_m$		$\mu$		$\log_{10}N_t$		$R$		$Z$	
			$(m^{-3}mm^{-1})$		$(mm)$				$(m^{-3})$		$(mm\ h^{-1})$		$dBZ$	
			ME	SD	ME	SD	ME	SD	ME	SD	ME	SD	ME	SD
S	LB	7123	3.42	0.42	0.96	0.21	11.48	7.98	1.98	0.38	0.54	0.60	16.93	5.93
	HS	12694	3.60	0.44	0.88	0.21	11.24	7.89	2.14	0.40	0.54	0.58	16.17	6.06
	TL	10091	3.71	0.43	0.87	0.20	11.90	8.01	2.23	0.39	0.65	0.67	16.85	6.15
	SD	7175	3.51	0.44	0.95	0.22	11.15	8.03	2.07	0.39	0.62	0.64	17.36	6.10
	BLG	12467	3.72	0.49	0.88	0.23	12.24	8.50	2.25	0.44	0.70	0.74	17.11	6.33
	DLD	9685	3.70	0.42	0.88	0.21	11.91	7.91	2.23	0.38	0.67	0.69	17.18	6.13
C	LB	292	3.91	0.35	1.49	0.35	6.50	3.30	2.81	0.23	9.28	5.56	35.88	3.59
	HS	100	3.85	0.67	1.71	0.84	6.33	4.33	2.95	0.30	12.55	13.75	37.32	6.64
	TL	159	3.54	0.59	1.87	0.74	5.21	4.97	2.72	0.30	9.48	6.91	37.96	5.21
	SD	219	3.91	0.37	1.54	0.47	6.61	4.68	2.85	0.19	10.75	7.68	36.24	5.02
	BLG	198	3.91	0.74	1.64	0.97	8.00	7.37	3.00	0.27	10.57	15.49	36.29	6.75
	DLD	203	3.94	0.48	1.50	0.43	6.96	5.24	2.87	0.27	9.41	6.04	35.89	4.27
T	LB	787	3.76	0.39	1.15	0.21	8.37	4.35	2.47	0.31	2.16	1.25	26.42	3.89
	HS	541	3.89	0.49	1.05	0.29	8.98	6.74	2.59	0.33	1.81	1.15	24.79	3.89
	TL	465	3.77	0.70	1.22	0.49	8.81	6.91	2.56	0.44	2.30	1.21	27.10	4.39
	SD	819	3.87	0.41	1.12	0.26	8.23	5.46	2.59	0.28	2.28	1.18	26.59	4.04
	BLG	665	4.04	0.51	1.04	0.31	10.33	7.31	2.72	0.33	2.19	1.13	25.66	4.44
	DLD	503	3.95	0.46	1.10	0.30	8.69	6.16	2.67	0.31	2.35	1.17	26.60	4.20

444



445



446

Figure 9. As in Fig. 5 but for different rain types at six sites.

447

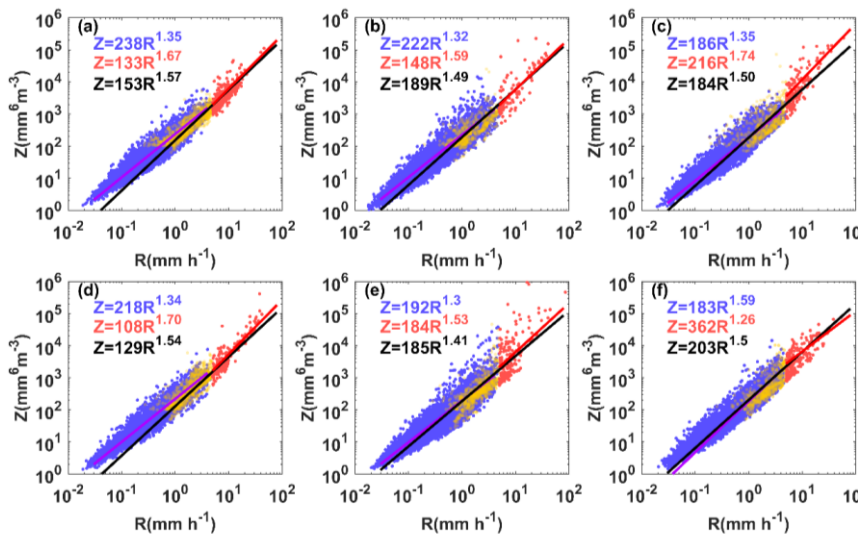
### 3.5 Implications for radar rainfall estimation with DSD

448

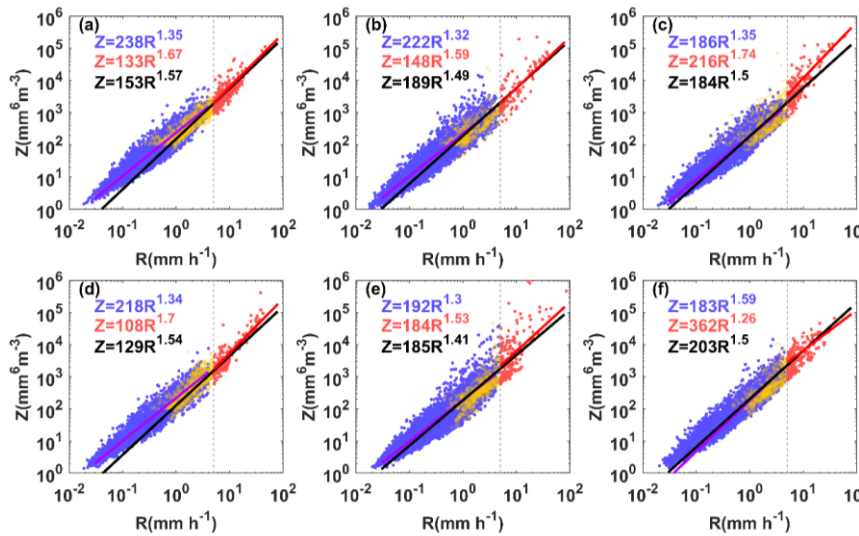
The sixth moment of raindrop diameter is proportional to the radar reflectivity

449 factor and the 3.76th moment is approximately the rain rate (they can be calculated by  
 450 Equations 4 and 5). Generally, the theoretical basis of QPE for single polarization radar  
 451 (ground-based or space-based) is the power relationship between the radar reflectivity  
 452 and rainfall rate ( $Z=AR^b$ ). This makes the coefficients  $A$  and exponents  $b$  of the power  
 453 relationship heavily dependent on the variation in DSD. Therefore, it is necessary to  
 454 obtain the  $A$  and  $b$  of different sites according to different rainfall types.

455 Figure 10-11 shows the  $Z$ - $R$  scatter plots for different sites and the fitted power-  
 456 law relationships for different rainfall types. The blue and red scatter points represent  
 457 stratiform and convective rainfall, respectively. The purple, red and black solid lines  
 458 indicate the  $Z$ - $R$  relationships for stratiform, convective and total rainfall, respectively.  
 459 It shows that the  $Z$ - $R$  scatter points for HS and BLG were relatively scattered around  
 460 the  $5 \text{ mm h}^{-1}$  rain rate. Besides, the  $Z$ - $R$  relationship of total rainfall underestimated the  
 461 stratiform rainfall at low  $R$  values and the convective rainfall at high  $R$  values. Based  
 462 on the average  $Z$ - $R$  relationship using a least-squares method, the dispersion degree of  
 463  $A$  and  $b$  at different sites was 42.5% and 10.7%, respectively, which reveals there to be  
 464 large differences in mountain areas.



465



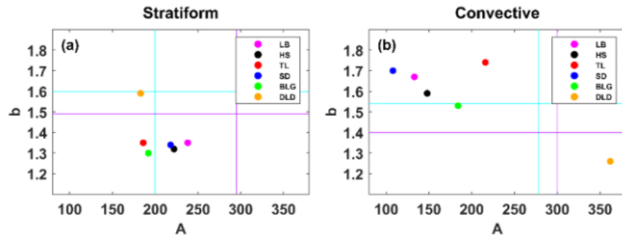
带格式的：居中

466

467 Figure 10.11. Scatter plots of  $Z$  ( $\text{mm}^6 \text{m}^{-3}$ ) versus  $R$  ( $\text{mm h}^{-1}$ ) for three rain types at (a)  
 468 LB, (b) HS, (c) TL, (d)SD, (e)BLG, and (f)DLD. The blue, red and yellow scatter points,  
 469 represent stratiform, convective and transitional cases, respectively. The purple, red and  
 470 black lines denote the  $Z$ - $R$  relationships. The blue, red and black formula denote stratiform,  
 471 convective and total  $Z$ - $R$  relationships. The grey dashed line indicates  $r$  is  $5 \text{ mmh}^{-1}$

带格式的：上标

472 In order to compare the six sites  $Z$ - $R$  relationships with some standard  $Z$ - $R$   
 473 relationships, the results for  $Z=300R^{1.4}$  for convective rainfall commonly used in radar,  
 474 and  $Z=200R^{1.6}$  (i.e., M48) for stratiform rainfall commonly used in midlatitude areas,  
 475 are provided in Figure 10.12. Overall, convective rainfall had smaller values of  $A$  and  
 476 larger values of  $b$  than those of stratiform rainfall (excluding DLD). The  $A$  values of  
 477 convective rainfall were smaller than the commonly used  $Z$ - $R$  relationship with large  
 478 differences, but the  $b$  values were greater. The distribution of  $A$  and  $b$  for stratiform  
 479 rainfall was relatively concentrated, with  $A$  and  $b$  ranging from 186–238 and 1.3–1.35,  
 480 respectively. The  $A$  values of stratiform rainfallSR were close to those of M48, and the  
 481  $b$  values were close to and smaller than the  $Z$ - $R$  of global stratiform rainfallSR.  
 482 StationSite DLD had a similar  $Z$ - $R$  for stratiform rainfall with as M48, while its  
 483 convective rainfall was different from other sites, with a larger  $A$  value (twice as large  
 484 as other sites) and smaller  $b$  value, which probably relates to its own local climatic  
 485 influences formed in a narrow valley. In addition, it is clear that the  $A$  value of stratiform  
 486 rainfall increased from the southern slopes to northern slopes, while the opposite was  
 487 the case for convective rainfall. Also, the  $Z$ - $R$  relationships of the same section are more  
 488 consistent, such as those of the interior or the northern slopes, which have distinct  
 489 geographic characteristics.



490  
 491 Figure 4. The  $A$  and  $b$  values of the  $Z$ - $R$  relationships for (a) stratiform rainfall and  
 492 (b) convective rainfall at six sites. The purple lines in (a) and cyan lines in (b)  
 493 correspond to the global  $Z$ - $R$  model ( $Z = 295R^{1.49}$  for continental stratiform rainfall and  
 494  $Z = 278R^{1.54}$  for convective rainfall, respectively) (Ghada et al., 2018). The cyan lines  
 495 in (a) represent the midlatitude stratiform rainfall  $Z$ - $R$  model ( $Z = 200R^{1.60}$ , Marshall,  
 496 1948); and the purple lines in (b) represent the convective rainfall  $Z$ - $R$  model ( $Z =$   
 497  $300R^{1.40}$ ) applied to operational weather radar (Fulton et al., 1998).

#### 498 4 Discussion

499 The paper analyses the statistical characteristics of DSD at different sites in the  
 500 Qilian Mountains during the rainy season, which not only contain rainfall classes and  
 501 rainfall types but more importantly reflect the differences between different sites. The  
 502 results from different aspects can be mutually confirmed and have a good representation  
 503 of the spatial distribution, serving as a strong factual basis for discussion of the  
 504 microphysical structure of precipitation. For example, with the rain rate class rising, the  
 505 number concentration of all size bins is increased and the width of DSDs became wider,  
 506 which manifested as convective rainfall having a larger rain rate. In spatial terms, the  
 507 characteristics of precipitation in the interior of the mountains and on the southern  
 508 slopes were closer, whether considering the overall DSD distribution or the  
 509 distributions of DSD parameters. However, there were obvious variabilities at the  
 510 interior sites for DSD parameters due to the influences of local dynamics and thermal  
 511 effects. On the other hand, these characteristics also exhibited some differences between  
 512 the interior and eastern sections of the Qilian Mountains, especially in the discussion of  
 513 DSD parameters for rainfall classes and rainfall types (s Figures 5 and 9.10). This spatial  
 514 variation in DSD suggests that microphysical processes involved in the DSD are  
 515 influenced by complex topography (altitude, mountain alignment) and potentially  
 516 related to the source of water vapor, development of precipitation process and  
 517 anthropogenic factors.

518 Compared to previous studies that focused on eastern [3.48 for  $\log_{10}N_w$  and 1.23  
 519 mm for  $D_m$ , Pu et al.(2020)], southern [3.86 for  $\log_{10}N_w$  and 1.47 mm for  $D_m$ , Zhang et  
 520 al.(2019)], and northern [3.60 for  $\log_{10}N_w$  and 1.15 mm for  $D_m$ , Ma et al.(2019b)] and  
 521 central [3.48 for  $\log_{10}N_w$  and 1.54 mm for  $D_m$ , Fu et al.(2020)] China as well the Tibetan  
 522 Plateau [3.47 for  $\log_{10}N_w$  and 1.05 mm for  $D_m$ , Wang et al.(2021)], the Qilian Mountains  
 523 region has its own unique DSD characteristics and  $Z$ - $R$  relationship during the rainy  
 524 season, including a smaller raindrop diameter with a higher number concentration [3.69  
 525 for  $\log_{10}N_w$  and 0.94 mm for  $D_m$ ]. Moreover, the division of rainfall rate classes in the

带格式的: 字体: 倾斜

带格式的: 字体: 倾斜, 下标

带格式的: 字体: 倾斜

带格式的: 字体: 倾斜

带格式的: 字体: 倾斜

带格式的: 字体: 倾斜

带格式的: 字体: 倾斜



526 Qilian Mountains more adequately reflects the DSD characteristics in each class, unlike  
527 when using the classification method of other sites with larger rainfall rates. More  
528 importantly, the proposed classification of stratiform and convective rainfall can clearly  
529 distinguish between the distribution of  $\log_{10}N_w$  versus  $D_m$  in different rainfall types, for  
530 which the dividing line (slope of  $-1.6$  and intercept of  $6.008$ ) between stratiform and  
531 convective rainfall has the same slope as the line (slope of  $-1.6$  and intercept of  $6.3$ )  
532 given by Bringi et al (2003). Furthermore, according to this method, it can be easily  
533 proven that convective events are more consistent with the not belong to the continental-  
534 like cluster or maritime-like cluster, conforming to the unique precipitation  
535 characteristics of the Qilian Mountains .

536 As mentioned above, the characteristics of DSD mainly describe diameters larger  
537 than  $0.2$  mm, which is limited by the observation instruments being unable to detect  
538 small drops of diameter less than  $0.2$  mm. Therefore, it is not a complete DSD, and the  
539 number concentration of small drops of diameter less than  $0.5$  mm is underestimated.  
540 Recent studies have been devoted to improving DSD observations in order to overcome  
541 the limitations of disdrometers. A study by Thurai et al. (2017) obtained a more  
542 complete DSD by splicing 2DVD and MPS (Meteorological Particle Spectrometer)  
543 measurements to observe DSDs and developed a technology to reconstruct the drizzle-  
544 mode DSD (Raupach et al., 2019), which a good presentation of the DSD of small  
545 raindrops was provided, and important applications were highlighted.

## 546 5 Summary and conclusion

547 Based on six months of DSD data observed over the southern slopes, northern  
548 slopes and interior of the Qilian Mountains, the characteristics and differences of DSD  
549 were studied, and the  $Z-R$  relationships of six sites were discussed. The main  
550 conclusions can be summarized as follows:  
551

- 552 1. For all rainfall events, the number concentrations of small and large raindrops in  
553 the interior and on the southern slopes were greater than that on the northern slopes,  
554 while midsize raindrops were less. The DSD of the interior of the mountains  
555 showed great variability, mainly in terms of the  $\log_{10}N_w$  and  $D_m$  (DSD parameters),  
556 which was quite different to the case for the northern slopes.
- 557 2. The rainfall rates were divided into six categories based on the DSD characteristics:  
558 C1,  $R < 0.5$ ; C2,  $0.5 \leq R < 2$ ; C3,  $2 \leq R < 4$ ; C4,  $4 \leq R < 6$ ; C5,  $6 \leq R < 10$ ; and C6,  $> 10$   
559  $\text{mm h}^{-1}$ . As the rainfall rate increased, the differences in number concentration of  
560 each raindrop size became significantly larger, especially at the interior sites.  
561 Besides, classes C5 and C6 made a relatively large contribution to the northern  
562 slopes, with a greater probability of heavy precipitation events.
- 563 3. The dispersion degree of  $\log_{10}N_w$  and  $D_m$  at the six sites was  $8.3\%$  and  $10.0\%$  for  
564 stratiform rainfall and  $10.4\%$  and  $23.4\%$  for convective rainfall, respectively. It is  
565 easier to increase the number concentration of large raindrops in the interior area  
566 of the mountains during convective rainfall. Meanwhile, there is a greater increase  
567 in the number concentration of raindrops over the northern slopes during  
568 convective rainfall.

569 4. The dispersion degree of coefficient  $A$  and exponent  $b$  in the  $Z$ - $R$  relationship for  
570 the six sites was 42.5% and 10.7%, respectively. Overall, the  $Z$ - $R$  relationships of  
571 the ipsilateral sites were more consistent; and the  $A$  value of stratiform rainfall  
572 increased from the southern slopes to northern slopes, while the opposite was true  
573 for convective rainfall. The  $Z$ - $R$  relationships in stratiform rainfall were similar  
574 and generally underestimated by the  $Z=200R^{1.6}$  model used for midlatitude  
575 stratiform rainfall; and the  $Z$ - $R$  relationships for convective precipitation varied  
576 greatly at different *stationsites*, which were overestimated by  $Z=300R^{1.4}$  at lower  
577 rain rates values and underestimated at higher rain rates values.

578 This study reveals the microphysical variability of precipitation over the complex  
579 topography of the arid and semi-arid regions of Northwest China, which can not only  
580 improve local numerical simulations, but also provides a basis for further understanding  
581 the differences in DSD characteristics formed at the mesoscale due to topographic  
582 factors and the water vapor distribution, etc. This study holds importance as a basis for  
583 the future implementation of weather modification techniques, which is of great  
584 significance in solving the shortage of water resources in the arid and semi-arid regions.

585 *Data availability.* Disdrometer data used in this study are available by contacting the  
586 authors.

587 *Author contributions.* WM conducted the detailed analysis; WZ provided financial  
588 support and conceived the idea; MK collated the observation data; all the authors  
589 contributed to the writing and revisions.

590 *Competing interests.* The authors declare that they have no conflict of interest.

#### 591 **Acknowledgments**

592 The work was supported by Weather modification ability construction project of  
593 Northwest China under grant No. ZQC-R18208 and The Second Tibetan Plateau  
594 Comprehensive Scientific Expedition Grant No. 2019QZKK0104. Thanks are given to  
595 Asi Zhang for her help in discussing some questions. The authors also thank reviewers  
596 and editors for their helpful suggestion for this study

597 **References**

- 598 Adirosi, E., N. Roberto, M. Montopoli, E. Gorgucci, and L. Baldini, 2018: Influence of  
599 disdrometer type on weather radar algorithms from measured DSD: Application  
600 to Italian climatology. *Atmosphere*, 9, 360.
- 601 Angulo-Martínez, M., and A. Barros, 2015: Measurement uncertainty in rainfall kinetic  
602 energy and intensity relationships for soil erosion studies: An evaluation using  
603 PARSIVEL disdrometers in the Southern Appalachian Mountains.  
604 *Geomorphology*, 228, 28-40.
- 605 Atlas, D., R. Srivastava, and R. S. Sekhon, 1973: Doppler radar characteristics of  
606 precipitation at vertical incidence. *Reviews of Geophysics*, 11, 1-35.
- 607 Bringi, V., V. Chandrasekar, J. Hubbert, E. Gorgucci, W. Randeu, and M. Schoenhuber,  
608 2003: Raindrop size distribution in different climatic regimes from disdrometer  
609 and dual-polarized radar analysis. *Journal of the atmospheric sciences*, 60, 354-  
610 365.
- 611 Campos, E., I. Zawadzki, M. Petitdidier, and W. Fernandez, 2006: Measurement of  
612 raindrop size distributions in tropical rain at Costa Rica. *Journal of Hydrology*,  
613 328, 98-109.
- 614 Chen, B., J. Yang, and J. Pu, 2013: Statistical characteristics of raindrop size  
615 distribution in the Meiyu season observed in eastern China. *Journal of the*  
616 *Meteorological Society of Japan. Ser. II*, 91, 215-227.
- 617 Dolan, B., B. Fuchs, S. Rutledge, E. Barnes, and E. Thompson, 2018: Primary modes  
618 of global drop size distributions. *Journal of the Atmospheric Sciences*, 75, 1453-  
619 1476.
- 620 Das, S., and A. Maitra, 2018: Characterization of tropical precipitation using drop size  
621 distribution and rain rate-radar reflectivity relation. *Theoretical and applied*  
622 *climatology*, 132, 275-286.
- 623 Fu, Z., and Coauthors, 2020: Statistical characteristics of raindrop size distributions and  
624 parameters in Central China during the Meiyu seasons. *Journal of Geophysical*  
625 *Research: Atmospheres*, 125, e2019JD031954.
- 626 Fulton, R. A., J. P. Breidenbach, D.-J. Seo, D. A. Miller, and T. O'Bannon, 1998: The  
627 WSR-88D rainfall algorithm. *Weather and forecasting*, 13, 377-395.
- 628 Geoffroy, O., A. Siebesma, and F. Burnet, 2014: Characteristics of the raindrop  
629 distributions in RICO shallow cumulus. *Atmospheric Chemistry and Physics*, 14,  
630 10897-10909.
- 631 Ghada, W., A. Buras, M. Lüpke, C. Schunk, and A. Menzel, 2018: Rain microstructure  
632 parameters vary with large-scale weather conditions in Lausanne, Switzerland.  
633 *Remote Sensing*, 10, 811.
- 634 Giannetti, F., and Coauthors, 2017: Real-time rain rate evaluation via satellite downlink  
635 signal attenuation measurement. *Sensors*, 17, 1864.
- 636 Gou, X., F. Chen, M. Yang, J. Li, J. Peng, and L. Jin, 2005: Climatic response of thick  
637 leaf spruce (*Picea crassifolia*) tree-ring width at different elevations over Qilian  
638 Mountains, northwestern China. *Journal of Arid Environments*, 61, 513-524.

639 Guyot, A., Pudashine, J., Protat, A., Uijlenhoet, R., Pauwels, V., Seed, A., and Walker,  
640 J. P., 2019: Effect of disdrometer type on rain drop size distribution  
641 characterisation: A new dataset for south-eastern Australia. *Hydrology and Earth  
642 System Sciences*, 23, 4737-4761.

643 [Han, H., Zhang, Y., Tian, J. et al. 2023: Raindrop Size Distribution Measurements at  
644 High Altitudes in the Northeastern Tibetan Plateau during Summer. \*Adv. Atmos.  
645 Sci.\* 40, 1244–1256.](#)

646 Jash, D., E. Resmi, C. Unnikrishnan, R. Sumesh, T. Sreekanth, N. Sukumar, and K.  
647 Ramachandran, 2019: Variation in rain drop size distribution and rain integral  
648 parameters during southwest monsoon over a tropical station: An inter-comparison  
649 of disdrometer and Micro Rain Radar. *Atmospheric Research*, 217, 24-36.

650 Jaffrain, J., and Berne, A., 2011: Experimental quantification of the sampling  
651 uncertainty associated with measurements from PARSIVEL disdrometers. *Journal  
652 of Hydrometeorology*, 12, 352-370.

653 Kruger, A., and W. F. Krajewski, 2002: Two-dimensional video disdrometer: A  
654 description. *Journal of Atmospheric and Oceanic Technology*, 19, 602-617.

655 Le Loh, J., D.-I. Lee, and C.-H. You, 2019: Inter-comparison of DSDs between  
656 Jincheon and Miryang at South Korea. *Atmospheric Research*, 227, 52-65.

657 Li, Z., and Coauthors, 2019: Climate background, relative rate, and runoff effect of  
658 multiphase water transformation in Qilian Mountains, the third pole region.  
659 *Science of The Total Environment*, 663, 315-328.

660 Lim, Y. S., J. K. Kim, J. W. Kim, B. I. Park, and M. S. Kim, 2015: Analysis of the  
661 relationship between the kinetic energy and intensity of rainfall in Daejeon, Korea.  
662 *Quaternary International*, 384, 107-117.

663 Ma, L., L. Zhao, D. Yang, Y. Xiao, L. Zhang, and Y. Qiao, 2019a: Analysis of Raindrop  
664 Size Distribution Characteristics in Permafrost Regions of the Qinghai–Tibet  
665 Plateau Based on New Quality Control Scheme. *Water*, 11, 2265.

666 Ma, Y., G. Ni, C. V. Chandra, F. Tian, and H. Chen, 2019b: Statistical characteristics of  
667 raindrop size distribution during rainy seasons in the Beijing urban area and  
668 implications for radar rainfall estimation. *Hydrology and Earth System Sciences*,  
669 23, 4153-4170.

670 Marshall, J. S., 1948: The distribution of raindrops with size. *J. meteor.*, 5, 165-166.

671 McFarquhar, G. M., T.-L. Hsieh, M. Freer, J. Mascio, and B. F. Jewett, 2015: The  
672 characterization of ice hydrometeor gamma size distributions as volumes in  $N_0$ –  
673  $\lambda$ – $\mu$  phase space: Implications for microphysical process modeling. *Journal of  
674 Atmospheric Sciences*, 72, 892-909.

675 Narayana Rao, T., N. Kirankumar, B. Radhakrishna, and D. Narayana Rao, 2006: On  
676 the variability of the shape-slope parameter relations of the gamma raindrop size  
677 distribution model. *Geophysical research letters*, 33.

678 Protat, A., and Coauthors, 2019: The latitudinal variability of oceanic rainfall properties  
679 and its implication for satellite retrievals: 1. Drop size distribution properties.  
680 *Journal of Geophysical Research: Atmospheres*, 124, 13291-13311.

- 681 Pu, K., X. Liu, Y. Wu, S. Hu, L. Liu, and T. Gao, 2020: A comparison study  
682 of raindrop size distribution among five sites at the urban scale during the  
683 East Asian rainy season. *Journal of Hydrology*, 590, 125500, <https://doi.org/10.1016/j.jhydrol.2020.125500>.  
684
- 685 Penide, G., A. Protat, V. V. Kumar, and P. T. May, 2013: Comparison of two  
686 convective/stratiform precipitation classification techniques: Radar reflectivity  
687 texture versus drop size distribution–based approach. *Journal of Atmospheric and*  
688 *Oceanic Technology*, 30, 2788-2797.
- 689 Qin, Y., H. Lei, D. Yang, B. Gao, Y. Wang, Z. Cong, and W. Fan, 2016: Long-term  
690 change in the depth of seasonally frozen ground and its ecohydrological impacts  
691 in the Qilian Mountains, northeastern Tibetan Plateau. *Journal of Hydrology*, 542,  
692 204-221.
- 693 Rincon, R. F., and R. H. Lang, 2002: Microwave link dual-wavelength measurements  
694 of path-average attenuation for the estimation of drop size distributions and rainfall.  
695 *IEEE Transactions on geoscience and remote sensing*, 40, 760-770.
- 696 Raupach, T. H., M. Thurai, V. Bringi, and A. Berne, 2019: Reconstructing the drizzle  
697 mode of the raindrop size distribution using double-moment normalization.  
698 *Journal of Applied Meteorology and Climatology*, 58, 145-164.
- 699 Seela, B. K., J. Janapati, P. L. Lin, K. K. Reddy, R. Shirooka, and P. K. Wang, 2017: A  
700 comparison study of summer season raindrop size distribution between Palau and  
701 Taiwan, two islands in western Pacific. *Journal of Geophysical Research:*  
702 *Atmospheres*, 122, 11,787-711,805.
- 703 Smith, J. A., E. Hui, M. Steiner, M. L. Baeck, W. F. Krajewski, and A. A. Ntelekos,  
704 2009: Variability of rainfall rate and raindrop size distributions in heavy rain.  
705 *Water Resources Research*, 45.
- 706 Thurai, M., P. Gatlin, and V. Bringi, 2016: Separating stratiform and convective rain  
707 types based on the drop size distribution characteristics using 2D video  
708 disdrometer data. *Atmospheric Research*, 169, 416-423.
- 709 Thurai, M., P. Gatlin, V. Bringi, W. Petersen, P. Kennedy, B. Notaroš, and L. Carey,  
710 2017: Toward completing the raindrop size spectrum: Case studies involving 2D-  
711 video disdrometer, droplet spectrometer, and polarimetric radar measurements.  
712 *Journal of Applied Meteorology and Climatology*, 56, 877-896.
- 713 Testud, J., S. Oury, R. A. Black, P. Amayenc, and X. Dou, 2001: The concept of  
714 “normalized” distribution to describe raindrop spectra: A tool for cloud physics  
715 and cloud remote sensing. *Journal of Applied Meteorology*, 40, 1118-1140.
- 716 Tian, H., T. Yang, and Q. Liu, 2014: Climate change and glacier area shrinkage in the  
717 Qilian mountains, China, from 1956 to 2010. *Annals of Glaciology*, 55, 187-197.
- 718 [Tokay A, Wolff D B, Petersen W A, 2014. Evaluation of the New Version of the Laser-](#)  
719 [Optical Disdrometer. \*OTT Parsivel\*?. \*Journal of atmospheric and oceanic\*](#)  
720 [technology, 31, 1276-1288.](#)
- 721 Ulbrich C W., 1983: Natural variations in the analytical form of the raindrop size  
722 distribution. *Journal of climate and applied meteorology*, 22, 1764-1775.

带格式的: 字体: Times New Roman, 字体颜色: 自动设置

带格式的: 字体: Times New Roman, 小四, 字体颜色: 自动设置, 上标

723 Wainwright, C. E., D. T. Dawson, M. Xue, and G. Zhang, 2014: Diagnosing the  
724 intercept parameters of the exponential drop size distributions in a single-moment  
725 microphysics scheme and impact on supercell storm simulations. *Journal of*  
726 *Applied Meteorology and Climatology*, 53, 2072-2090.

727 Wang, Y., J. Zheng, Z. Cheng, and B. Wang, 2020: Characteristics of Raindrop Size  
728 Distribution on the Eastern Slope of the Tibetan Plateau in Summer. *Atmosphere*,  
729 11, 562.

730 Wu, Y., and L. Liu, 2017: Statistical characteristics of raindrop size distribution in the  
731 Tibetan Plateau and southern China. *Advances in Atmospheric Sciences*, 34, 727-  
732 736.

733 Yang, L., J. Smith, M. L. Baeck, B. Smith, F. Tian, and D. Niyogi, 2016: Structure and  
734 evolution of flash flood producing storms in a small urban watershed. *Journal of*  
735 *Geophysical Research: Atmospheres*, 121, 3139-3152.

736 Zhang, A., and Coauthors, 2019: Statistical characteristics of raindrop size distribution  
737 in the monsoon season observed in southern China. *Remote Sensing*, 11, 432.

738 Zhao, P., and Coauthors, 2019: The Tibetan Plateau surface-atmosphere coupling  
739 system and its weather and climate effects: The Third Tibetan Plateau Atmospheric  
740 Science Experiment. *Journal of Meteorological Research*, 33, 375-399.

741 Zeng, Y., and Coauthors, 2021: Statistical Characteristics of Raindrop Size Distribution  
742 during Rainy Seasons in Northwest China. *Advances in Meteorology*, 2021.  
743